J. Min. Metall. Sect. B-Metall. 57 (3) (2021) 331 - 340

Journal of Mining and Metallurgy, Section B: Metallurgy

THERMODYNAMIC ASSESSMENT OF THE Fe–Nb–Si SYSTEM

Y. Jiang [a,c], F. Li [a,*], S.-R. Li [b,], K. Xu [c,***], L.-L. Chen [c], Z.-X- Deng [c], Y.-Y Huang [c], K. Chang [c]**

[a] Shanghai Key Laboratory for High Temperature Materials and Precision Forming, Shanghai Jiao Tong University, Shanghai, China

[b] State Key Laboratory of Special Rare Metal Materials, Northwest Rare Metal Materials Research Institute Ningxia Co. Ltd., Shizuishan, China

[c] Key Laboratory of Marine Materials and Related Technologies, Zhejiang Key Laboratory of Marine Materials and Protective Technologies, Ningbo Institute of Materials Technology and Engineering, Chinese Academy of Sciences, Ningbo, Zhejiang, China

(Received 20 December 2019; Accepted 21 April 2021)

Abstract

Nb–Si based alloys have drawn continuously increasing attention due to their excellent high-temperature mechanical properties. The addition of element Fe could improve their poor high-temperature oxidation resistance which largely restricts their application. With the aim to study the effect of Fe addition on the Nb–Si system and to design appropriate alloy composition, the Fe–Nb–Si ternary system was thermodynamically investigated using the CALPHAD (CALculation of PHAse Diagrams) approach aided with the formation enthalpies for ternary compounds at 0 K computed via ab initio calculations. A self-consistent thermodynamic description of the Fe–Nb–Si system was obtained in this work. Key isothermal sections and liquidus projection were presented, and the calculation results showed a good agreement with available experimental data.

Keywords: *Fe–Nb–Si; Phase diagram; CALPHAD; Ab initio calculations*

1. Introduction

Nb–Si based alloys attract great attention for their high melting point, low density and excellent high-temperature mechanical properties, which makes them candidates for the next generation of turbine airfoil materials [1-6]. However, room temperature brittleness and poor high-temperature oxidation resistance restrict their applications. It is reported that the addition of Fe element could improve the high-temperature oxidation resistance of the Nb–Si alloys [7]. On the other side, Fe–Si based alloys (silicon steels) are excellent soft magnetic materials and have been widely applied in motors and transformers [8]. With the increase of market demand for silicon steels, further improvement to achieve a higher permeability and lower power losses is required [9]. Alloying with carbonitride formers, such as Nb and Ti [10-14], has been recognized as a crucial mechanism to obtain enhanced properties for silicon steels. In other words, the Fe–Nb–Si system is also an important subsystem for the silicon steels.

Thermodynamic calculation in the frameworks of the CALPHAD (CALculation of PHAse Diagrams) approach allows to spare time and efforts required to design new materials [15-17]. The Fe–Nb–Si system has been experimentally investigated several times [18-30]. The obtained experimental data are used as the basis of thermodynamic calculations. *Ab initio* calculations are used to obtain the formation enthalpies of the ternary compounds in this system in order to provide reliable end-members during optimization. The purpose of this study was to obtain a set of self-consistent parameters to describe the Fe–Nb–Si system and provide theoretical basis of thermodynamics for alloy design.

2. Literature review

2.1. The Fe–Nb system

There are two intermetallic phases, $\varepsilon NbFe_2$ and μFeNb, and four solid solution phases (δFe), (γFe), (αFe), and (Nb) in the Fe–Nb system, as listed in Table 1 [31]. Huang [32] first assessed the Fe–Nb system where the ε phase was treated as stoichiometric phase and the homogeneity range of the μ phase was limited with a congruent melting, which was inconsistent with the later experimental

Corresponding author: lifei74@sjtu.edu.cn [*]; lishr@otic.com.cn [**]; xukaikai@nimte.ac.cn [***]

https://doi.org/10.2298/JMMB191220029J

data. In later studies, many researchers re-assessed this system by using different sublattice models for the ε or μ phase to fit the available experimental data [33-36].

Liu et al. [37] optimized the Fe–Nb system where *ab initio* calculations were used to obtain the formation enthalpies of the ε and μ phases at 0 K. Subsequently, Khvan et al. [38, 39] re-assessed this system twice in order to describe the solubility of Nb in the Fcc phase reasonably. In the present work, the parameters from Khvan et al. [39] were adopted and the calculated phase diagram is shown in Fig. 1a.

2.2. The Fe–Si system

There are five intermetallic phases Fe_2Si, Fe_5Si_3, FeSi, $FeSi_2$, and Fe_3Si_7 and three solid solution phases (αFe), (γFe), and (Si) in the Fe–Si system, as listed in Table 1 [40]. The Fe–Si phase diagram is one of the most complicated binary phase diagrams because the Fe rich part of this system involves the low temperature magnetic transition, A2/B2 transition, and B2/$D0_3$ transition. In the early report, Lacaze and Sundman [41] assessed the Fe–Si system including the A2/B2 ordering reaction of the Bcc phase, but the B2/$D0_3$ transition was neglected. Subsequently, Miettinen [42] proposed new values for the interaction parameter of the liquid phase for a better modeling of the Fe–Si–C system based on the work by Lacaze and Sundman [41]. Ohnuma et al. [43] experimentally investigated the Fe–Si system and carried out a new assessment. Recently, Cui and Jung [44] re-optimized the Fe–Si system and obtained two sets of model parameters with MQM and BW, where both the A2/B2 transition and B2/$D0_3$ transition were considered. Since the evaluation of Lacaze and Sundman [41] showed good agreement with experimental data and has been widely accepted, the thermodynamic assessment of the system by Lacaze and Sundman [41] was adopted, and the calculated Fe–Si phase diagram is shown in Fig. 1b.

2.3. The Nb–Si system

There are four intermetallic phases Nb_3Si, αNb_5Si_3, βNb_5Si_3, and $NbSi_2$ and two solid solution phases (Nb) and (Si) in the Nb–Si system, as listed in Table 1 [45]. The thermodynamic description of the Nb–Si system has been established by many researchers [46-56]. In the early reports, all the intermetallic compounds of the Nb–Si system were regarded as stoichiometric phases due to the negligible solubility ranges [45, 46, 57]. Fernandes et al. [47] first calculated this system considering the solubility of βNb_5Si_3. Then, David et al. [51] re-modeled αNb_5Si_3 and $NbSi_2$ as non-stoichiometric phases. The related transformations βNb_5Si_3+Nb_3Si↔αNb_5Si_3 and βNb_5Si_3↔αNb_5Si_3+$NbSi_2$ were re-described and widely accepted by later researchers. Based on the work of David et al. [51], Geng et al. [52] modified the Nb–Si system in order to match the experiments and thermodynamic data better. In the present work, the parameters reported by Geng et al. [52] were adopted, and the calculated Nb–Si phase diagram is shown in Fig. 1c.

2.4. The Fe–Nb–Si system

The Fe–Nb–Si ternary system has not been thermodynamically assessed yet. Goldschmidt et al. [18] studied the Fe–Nb–Si system by X-ray diffraction (XRD) analysis using the powder-photography of alloys in equilibrium at 1273K. They showed the existence of at least six, possible nine ternary compounds, but their crystal structures were unknown. Gladyshevskii and Kuz'ma [22] determined one of these to be Nb_4FeSi (τ_4), exhibiting the structure of $CuAl_2$ type. As listed in Table 1, another five ternary phases, viz. $Nb_4Fe_4Si_7$ (τ_5), NbFeSi (τ_6), $NbFeSi_2$ (τ_1), Nb_2FeSi_2 (τ_2), and $Nb_4Fe_3Si_5$ (τ_3) were confirmed in later years [19-21].

Denham [26] found that the extent of the Laves field in the Fe–Nb–Si system was similar at 1273K and 1573K but smaller than previously reported. Singh and Gupta [27] reported a partial isothermal section at 1373K based on the experimental results. However, the homogeneity ranges of Laves phase and μ phase were fairly large, and both extended along constant niobium lines. Raghavan and Ghosh [28] gave a tentative isothermal section at 1423K, where the six ternary compounds were considered and the extent of the ternary Laves phase region was consistent with that given by Denham and Singh [26]. Combining the results of Goldschmidt [18] and Haour [30], and the binary data [31, 40, 45], a tentative liquidus projection was also constructed by Raghavan and Ghosh [28].

Wang et al. [58] investigated the Fe–Nb–Si system by electron probe microanalyzer (EPMA), back scattered electron (BSE), XRD, and differential scanning calorimetry (DSC). They confirmed six ternary compounds and established three isothermal sections at 1473, 1373, and 1273K, respectively.

3. Thermodynamic models

3.1. Unary phases

The Gibbs energy function ${}^0G_i^{\varphi}(T) = G_i^{\varphi}(T) - H_i^{SER}$ for element *i* (*i*=Fe, Nb, Si) in the phase φ (φ=Liquid, (δFe), (Nb), etc.) is expressed by the following equation:

$$ {}^0G_i^{\varphi}(T) = a + b\times T + c\times T\times \ln T + d\times T^2 + e\times T^{-1} + f\times T^3 + g\times T^7 + h\times T^{-9} \quad (1) $$

where: H_i^{SER} is the molar enthalpy of formation of

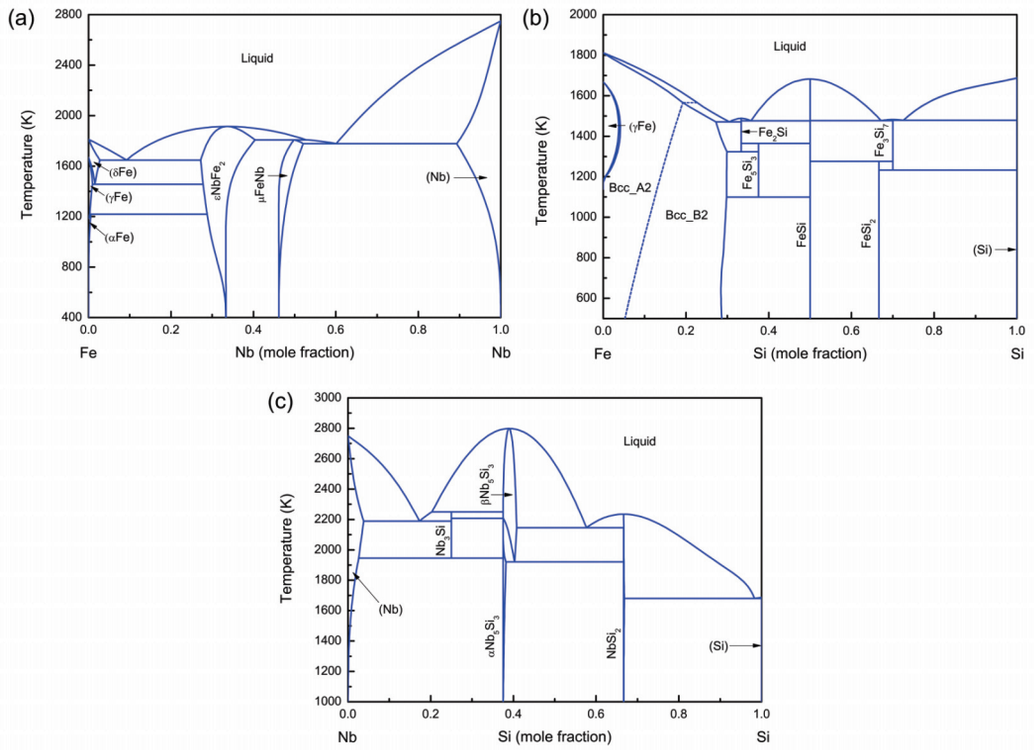

Figure 1. *The calculated phase diagrams of the (a) Fe–Nb [39], (b) Fe–Si [41] and (c) Nb–Si [52] binary systems*

the element *i* in its stable reference state at 298.15 K and atmospheric pressure (101325 Pa), and *T* is the absolute temperature. The Gibbs energy functions for Fe, Nb, and Si were taken from the Scientific Group Thermodata Europe (SGTE) database compiled by Dinsdale [59].

3.2. Solution phases

The molar Gibbs free energies for (αFe), (γFe), (δFe), (Nb), and (Si), modeled as substitutional solutions, are described by the following equation:

$$G_m^{\varphi} - H^{SER} = \sum_{i=1}^{n} x_i {}^0G_i^{\varphi} + RT\sum_{i=1}^{n} x_i \ln(x_i) + {}^{ex}G^{\varphi} \quad (2)$$

where: ${}^0G_i^{\varphi}$ is the molar Gibbs free energy of pure element *i* in the phase φ, x_i is the mole fraction of the components *i*, the term ${}^{ex}G^{\varphi}$ is the excess free energy, which is expressed by the Redlich-Kister polynomial [60] as:

$${}^{ex}G^{\varphi} = x_{Fe}x_{Nb}L^{\varphi}_{Fe,Nb} + x_{Fe}x_{Si}L^{\varphi}_{Fe,Si} + x_{Nb}x_{Si}L^{\varphi}_{Nb,Si} + x_{Fe}x_{Nb}x_{Si}L^{\varphi}_{Fe,Nb,Si} \quad (3)$$

$$L^{\varphi}_{i,j} = \sum_{m=0}^{n} {}^mL^{\varphi}_{i,j}(x_i - x_j)^m \quad (4)$$

$$L^{\varphi}_{Fe,Nb,Si} = x_{Fe}\,{}^0L^{\varphi}_{Fe,Nb,Si} + x_{Nb}\,{}^1L^{\varphi}_{Fe,Nb,Si} + x_{Si}\,{}^2L^{\varphi}_{Fe,Nb,Si} \quad (5)$$

$${}^nL^{\varphi}_{Fe,Nb,Si} = a + b \times T (n = 0,1,2) \quad (6)$$

where: $L^{\varphi}_{i,j}$ is the interaction parameter in the *i-j* binary system, ${}^nL^{\varphi}_{Fe,Nb,Si}$ is the ternary interaction parameter, and its coefficients *a* and *b* are to be evaluated in the present work.

3.3. Binary phases extending into the ternary system

Sublattice models were used to describe the following binary phases with solubilities for the third elements: $(Nb, Si, Fe)_5(Si, Fe)_3$ for αNb_5Si_3, $(Fe, Nb)_1(Fe, Nb, Si)_2$ for $\varepsilon NbFe_2$, and $(Fe, Nb)_1(Nb)_4(Fe, Nb)_2(Fe, Nb, Si)_6$ for μFeNb. The Gibbs free energy of αNb_5Si_3 phase is expressed as the following:

$$\begin{aligned} {}^0G_m^{\varphi} &= \sum_i \sum_j y_i' y_i'' G^{\varphi}_{i:j} \\ &+ RT(5\sum_i y_i' \ln y_i' + 3\sum_j y_j'' \ln y_j'') \\ &+ \sum_m \sum_n \sum_j y_m' y_n' y_j'' {}^0L^{\varphi}_{m,n:j} + \sum_i y_i' y_{Si}'' y_{Fe}'' {}^0L^{\varphi}_{i:Si,Fe} \end{aligned} \quad (7)$$

where: y_i' and y_j'' (*i*=Nb, Si, Fe and *j*=Si, Fe, the same below) are the site fraction of the components in the first and second sublattice, respectively, and $G^{\varphi}_{i:j}$ is the molar Gibbs energy of the end-member in the phase φ. The subscripts *m* and *n* can be Nb, Si, and Fe, but $m \neq n$. ${}^0L^{\varphi}_{m,n:j}$ is the interaction parameter between *m* and *n* in the first sublattice, while the second sublattice is occupied by *j*. The interaction between two species in one sublattice was assumed to be independent of the occupation of the other sublattice.

Table 1. *Crystal structures of phases in the Fe–Nb–Si system*

Phase	Prototype	Peasrson's symbol	Space group	References
(Nb)	W	*cI*2	*Im*-3*m*	[45]
(Si)	C(diamond)	*cF*8	*Fd*-3*m*	[45]
(αFe)/(δFe)	W	*cI*2	*Im*-3*m*	[31]
(γFe)	Cu	*cF*4	*Fm*-3*m*	[31]
$\varepsilon NbFe_2$	$MgZn_2$	*hP*12	$P6_3/mmc$	[31]
μFeNb	Fe_7W_6	*hR*13	*R*-3*m*	[31]
Fe_5Si_3	Mn_5Si_3	*hP*16	$P6_3/mcm$	[40]
Fe_2Si	Fe_2Si	*hP*6	*P*-3*m*1	[40]
FeSi	FeSi	*cP*8	$P2_13$	[40]
$FeSi_2$	$FeSi_2$	*tP*3	*P*4/*mmm*	[40]
Fe_3Si_7	$FeSi_2$	*oC*48	*Cmca*	[40]
αNb_5Si_3	Cr_5B_3	*tI*32	*I*4/*mcm*	[45]
βNb_5Si_3	W_5Si_3	*tI*32	*I*4/*mcm*	[45]
Nb_3Si	Ti_3P	*tP*32	$P4_2/n$	[45]
$NbSi_2$	$CrSi_2$	*hP*9	$P6_422$	[45]
$NbFeSi_2$ (τ_1)	$TiMnSi_2$ or $TiFeSi_2$	*Orthorhombic*	*Pbam*	[19]
Nb_2FeSi_2 (τ_2)		*tetragonal*	$P4_2/mcm$	[20]
$Nb_4Fe_3Si_5$ (τ_3)		*Orthorhombic*	$P2_1mn$	[21]
Nb_4FeSi (τ_4)	Al_2Cu	*tI*12	*I*4/*mcm*	[22]
$Nb_4Fe_4Si_7$ (τ_5)	$Zr_4Co_4Ge_7$	*tetragonal*	*I*4/*mmm*	[23, 24]
NbFeSi (τ_6)	TiNiSi or $PbCl_2$	*oP*12	*pnma*	[24, 25]

Analogous expressions were used to describe the Gibbs energies of $\varepsilon NbFe_2$ and μFeNb phases.

3.4. Ternary compounds

The $NbFeSi_2$, Nb_2FeSi_2, $Nb_4Fe_3Si_5$, Nb_4FeSi, $Nb_4Fe_4Si_7$, and NbFeSi phases were described as stoichiometric compounds. The molar Gibbs free energies of these phases can be expressed as:

$$^0G_m^{Nb_xSi_yFe_z} - x \times H_{Nb}^{SER} - y \times H_{Si}^{SER} - z \times H_{Fe}^{SER} = a + b \times T + x \times {}^0G_{Nb}^{bcc} + y \times {}^0G_{Si}^{diamond} + z \times {}^0G_{Fe}^{bcc} \quad (8)$$

in which the coefficients *a* and *b* were evaluated in the present work. The parameters $^0G_{Nb}^{bcc}$, $^0G_{Fe}^{bcc}$, and $^0G_{Si}^{diamond}$ were the Gibbs energies of (Nb), (αFe), and (Si), respectively.

4. Results and discussion

Since no experimental data for the ternary compounds were available in the Fe–Nb–Si system, *ab initio* calculations were employed. Formation enthalpies computed via *ab initio* calculations (Table 2) in this work were treated as end-members during thermodynamic optimization. On the basis of experimental isothermal sections at 1473, 1373, and 1273K, the Fe–Nb–Si system was thermodynamically assessed in the present work and the thermodynamic models and optimized parameters are listed in Table 3. The optimization was conducted using the PARROT module of Thermo-Calc [61]. With these parameters, the isothermal sections at different temperatures and the liquidus projection are calculated and presented as follows.

In the present work, all the thermodynamic parameters were optimized using the PARROT module of Thermo-Calc [61]. The step-by-step optimization method was used [62, 63]. Firstly, as for the binary Fe–Zr, Nb–Zr, and Si–Zr systems, the thermodynamic model of $\varepsilon NbFe_2$, μFeNb, and αNb_5Si_3 phases was adjusted to describe their ternary solubilities. Secondly, all the ternary stoichiometric phases, $NbFeSi_2$, Nb_2FeSi_2, $Nb_4Fe_3Si_5$, Nb_4FeSi, $Nb_4Fe_4Si_7$, and NbFeSi phases, were added into the isothermal sections at 1423 K and 1473 K. Their thermodynamic parameters were optimized according to the experimental determined phase relationships. Thirdly, the experimental data on phase boundaries were used to optimize the thermodynamic parameters of the $\varepsilon NbFe_2$, μFeNb, and αNb_5Si_3 phases. A set of thermodynamic parameters for the Fe-Nb-Si system was finally obtained, as listed in Table 3.

4.1. Formation enthalpies computed via the ab initio calculations

Ab initio calculations based on the density functional theory (DFT) can provide insight into the characteristics of the thermodynamic and structural properties of phases, using only the atomic numbers and crystal structure information as input. The generalized gradient approximation (GGA) based on the Perdew-Burke-Ernzerhof (PBE) approach [64] for the exchange-correlation potential was employed. The valance electrons were explicitly treated by projector augmented plane-wave (PAW) potentials [65]. As implemented in the Vienna *ab initio* simulation package (VASP) [66]. A plane-wave cutoff energy of 550 eV and an energy convergence criterion of 10^{-5} eV for electronic structure self-consistency were used in the calculation. The integration in the Brillouin zone was done on the special *k*-points determined from the Monkhorst-Pack scheme [67]. The system was fully relaxed, including the unit cell sizes and the ionic coordinates, to find the stable state.

The formation enthalpy ΔH_f at 0 K for the compounds in the ternary system can be calculated by the following equation:

$$\Delta H_f(Nb_xSi_yFe_z) = E(Nb_xSi_yFe_z) - [x_{Nb}E(Nb) + x_{Si}E(Si) + x_{Fe}E(Fe)] \quad (9)$$

where $E(Nb_xSi_yFe_z)$, $E(Nb)$, $E(Si)$, and $E(Fe)$

denote the total energies of $Nb_xSi_yFe_z$, Nb, Si, and Fe at 0 K, respectively. x_i (i=Nb, Si or Fe) is the atomic fraction of the component. The reference states at 0 K are Bcc_A2, Diamond_A4 and Bcc_A2 for Nb, Si, and Fe, respectively. The calculated formation enthalpies for the ternary compounds are listed in Table 2.

Table 2 lists the lattice constants calculated by *ab initio* calculations compared with experimental data, and the calculated formation enthalpies from CALPHAD modeling compared with those from *ab initio* calculations. The information calculated by *ab initio* calculations from the well accepted Materials Project databases [63] are also listed in Table 2. Fig.2 shows the formation enthalpy of ternary compounds in the Fe–Nb–Si system calculated from *ab inito* and CALPHAD methods. The good agreement shows that the *ab initio* calculations generated data were reliable and could supplement the lack of experimental data.

4.2. Isothermal sections

Figs. 3-6 show the calculated isothermal sections at 1473, 1423, 1373, and 1273K compared with the experimental data reported by Wang [58] (Fig. 3b is a tentative isothermal section constructed by Raghavan

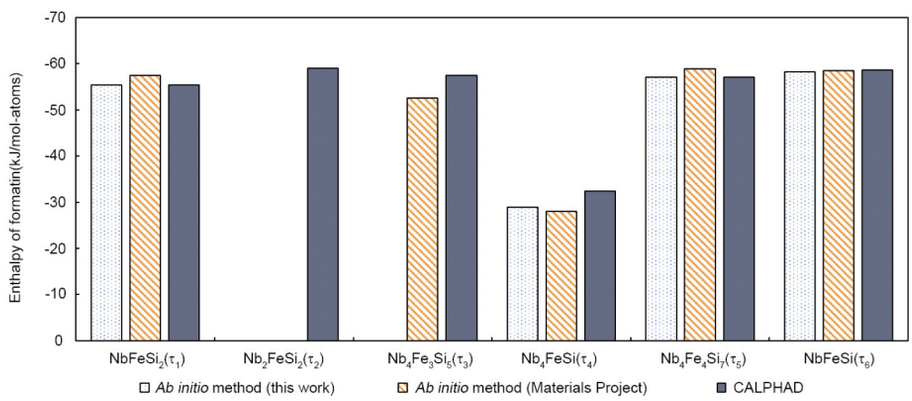

Figure 2. *Formation enthalpy of the Fe–Nb–Si ternary compounds calculated via the ab inito and CALPHAD approaches*

Table 2. *Summary of the lattice parameters and formation enthalpy of ternary compounds in the Fe–Nb–Si system*

Phase	Lattice parameters (Å)			Formation enthalpy (kJ/mol-atoms)		Atomic number	*k*-points	References
	a	b	c	*Ab initio* method	CALPHAD	(uint cell)		
$NbFeSi_2$ (τ_1)	7.558	8.700	9.719	-55.44	-55.44	48	7×7×7	This work
	7.576	9.733	8.689	–	–			[19]
	7.568	8.696	9.684	-57.41				Materials Project [63]
Nb_2FeSi_2 (τ_2)	–	–	–	–	-59.00			This work
	23.76		4.959	–	–			[20]
$Nb_4Fe_3Si_5$ (τ_3)	–	–	–	–	-57.50			This work
	12.821	4.912	15.521	–	–			[21]
	4.946	8.460	7.660	-52.59				Materials Project [63]
Nb_4FeSi (τ_4)	6.182	6.182	5.111	-28.93	-32.33	12	9×9×9	This work
	6.193	6.193	5.056	–	–			[22]
	6.195	6.195	5.096	-27.98				Materials Project [63]
$Nb_4Fe_4Si_7$ (τ_5)	dec-59	dec-59	5.031	-57.07	-57.07	60	5×5×11	This work
	12.652	12.652	4.981	–	–			[24]
	12.591	12.591	5.004	-58.86				Materials Project [63]
NbFeSi (τ_6)	3.732	6.224	7.022	-58.24	-58.67	12	7×9×11	This work
	6.231	3.677	7.190	–	–			[24]
	3.605	9.198	4.954	-58.47				Materials Project [63]

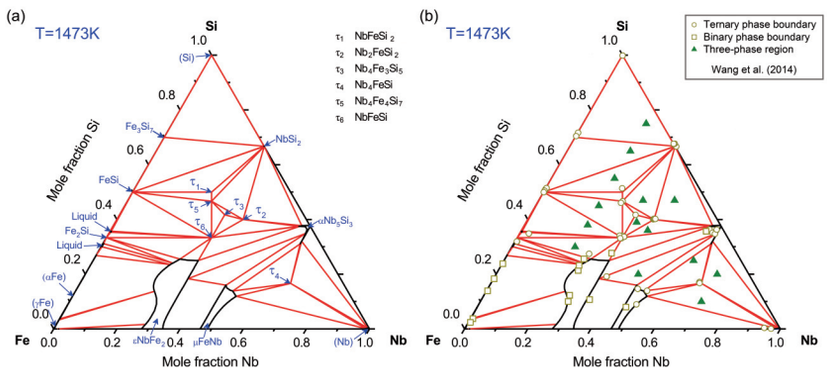

Figure 3. *Isothermal sections of the Fe–Nb–Si system at 1473K: (a) calculated isothermal section; (b) comparison between the calculated isothermal sections and the experimental data [58]*

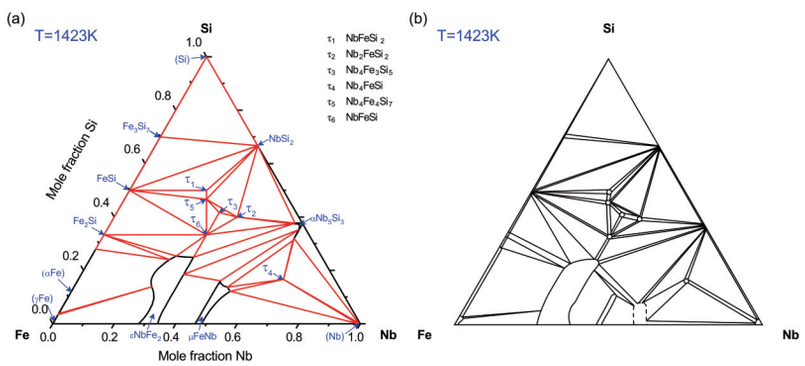

Figure 4. *Isothermal sections of the Fe–Nb–Si system at 1423K: (a) calculated isothermal section; (b) tentative isothermal section by Raghavan [28]*

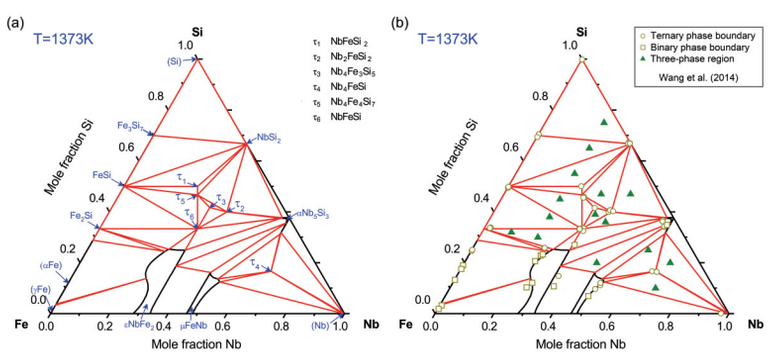

Figure 5. *Isothermal sections of the Fe–Nb–Si system at 1373K: (a) calculated isothermal section; (b) comparison between the calculated isothermal sections and the experimental data [58]*

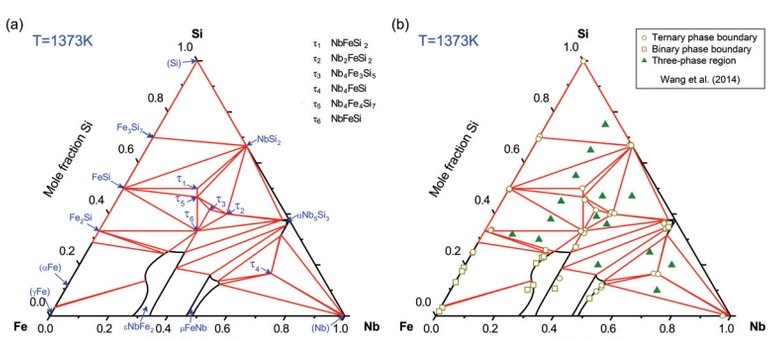

Figure 6. *Isothermal sections of the Fe–Nb–Si system at 1273K: (a) calculated isothermal section; (b) comparison between the calculated isothermal sections and the experimental data [58]*

Table 3. *Summary of the thermodynamic parameters in the Fe–Nb–Si system*

Phases	Models	Parameters
$\varepsilon NbFe_2$	$(Fe, Nb)_1(Fe, Nb, Si)_2$	${}^0G^{\varepsilon NbFe_2}_{Fe:Si} = {}^0G^{BCC}_{Fe} + 2\,{}^0G^{DIAMOND}_{Si} + 161798.15$
		${}^0G^{\varepsilon NbFe_2}_{Nb:Si} = {}^0G^{BCC}_{Fe} + 2\,{}^0G^{DIAMOND}_{Si} + 27259.15$
		${}^0L^{\varepsilon NbFe_2}_{Fe:Fe,Si} = -500000$
		${}^0L^{\varepsilon NbFe_2}_{Nb:Fe,Si} = -580000$
μFeNb	$(Fe, Nb)_1(Nb)_4(Fe, Nb)_2(Fe, Nb, Si)_6$	${}^0G^{\mu FeNb}_{Fe:Nb:Nb:Si} = {}^0G^{BCC}_{Fe} + 6\,{}^0G^{BCC}_{Nb} + 6\,{}^0G^{DIAMOND}_{Si} - 356484.1$
		${}^0L^{\mu FeNb}_{Fe:Nb:Nb:Fe,Si} = -1400000$
		${}^0L^{\mu FeNb}_{Fe:Nb:Nb:Nb,Si} = -1300000$
αNb_5Si_3	$(Fe, Nb, Si)_5(Fe, Si)_3$	${}^0G^{\alpha Nb_5Si_3}_{Fe:Si} = 5\,{}^0G^{BCC}_{Fe} + 3\,{}^0G^{DIAMOND}_{Si}$
		${}^0G^{\alpha Nb_5Si_3}_{Nb:Si} = 5\,{}^0G^{BCC}_{Nb} + 3\,{}^0G^{DIAMOND}_{Si}$
		${}^0G^{\alpha Nb_5Si_3}_{Si:Fe} = 5\,{}^0G^{DIAMOND}_{Si} + 3\,{}^0G^{BCC}_{Fe}$
		${}^0G^{\alpha Nb_5Si_3}_{Fe:Fe} = 0$
		${}^0L^{\alpha Nb_5Si_3}_{Fe,Nb:Si} = -300000$
		${}^0L^{\alpha Nb_5Si_3}_{Nb:Fe,Si} = -150000$
$NbFeSi_2$	$(Nb)(Fe)(Si)_2$	${}^0G^{NbFeSi_2}_{Nb:Fe:Si} = {}^0G^{BCC}_{Nb} + {}^0G^{BCC}_{Fe} + 2\,{}^0G^{DIAMOND}_{Si} - 221753.7$
Nb_4FeSi	$(Nb)_4(Fe)(Si)$	${}^0G^{Nb_4FeSi}_{Nb:Fe:Si} = 4\,{}^0G^{BCC}_{Nb} + {}^0G^{BCC}_{Fe} + {}^0G^{DIAMOND}_{Si} - 194000 - 33T$
$Nb_4Fe_4Si_7$	$(Nb)_4(Fe)_4(Si)_7$	${}^0G^{Nb_4Fe_4Si_7}_{Nb:Fe:Si} = 4\,{}^0G^{BCC}_{Nb} + 4\,{}^0G^{BCC}_{Fe} + 7\,{}^0G^{DIAMOND}_{Si} - 856079.14$
NbFeSi	(Nb)(Fe)(Si)	${}^0G^{NbFeSi}_{Nb:Fe:Si} = {}^0G^{BCC}_{Nb} + {}^0G^{BCC}_{Fe} + {}^0G^{DIAMOND}_{Si} - 176000 - 3.8T$
$Nb_4Fe_3Si_5$	$(Nb)_4(Fe)_3(Si)_5$	${}^0G^{Nb_4Fe_3Si_5}_{Nb:Fe:Si} = 4\,{}^0G^{BCC}_{Nb} + 3\,{}^0G^{BCC}_{Fe} + 5\,{}^0G^{DIAMOND}_{Si} - 690000 - 26T$
Nb_2FeSi_2	$(Nb)_2(Fe)(Si)_2$	${}^0G^{Nb_2FeSi_2}_{Nb:Fe:Si} = 2\,{}^0G^{BCC}_{Nb} + {}^0G^{BCC}_{Fe} + 2\,{}^0G^{DIAMOND}_{Si} - 295000 - 17.2T$

[28]). Three binary phases ($\varepsilon NbFe_2$, μFeNb, and αNb_5Si_3) were calculated to have obvious ternary solid solubilities. Six ternary compounds (τ_1, τ_2, τ_3, τ_4, τ_5, and τ_6) were obtained at these temperatures.

The main difference between the calculated phase diagrams and experimental measurements was the single-phase region of μFeNb. According to [58], the solubility of Si in the μFeNb phase decreased from 14.7 at.% to 10.0 at.% with temperature decreasing from 1473K to 1273K. But in the present work, the morphology of μFeNb phase region mainly stayed the same as temperature ranged from 1473K to 1273K, which conflicted with the experimental data. It may be attributed to the thermodynamic parameter of μFeNb phase. Generally, the calculated results had good agreement with the experimental data.

4.3. Liquidus projection and invariant reaction scheme

The calculated liquidus projection with nineteen primary phases regions is shown in Fig. 7. There were twenty-one eutectic grooves, eighteen peritectic ridges, and eleven saddle points. Sixteen transitional invariant reactions and seven eutectic reactions were involved in the Fe–Nb–Si ternary system. The reaction scheme for the liquidus projection of the Fe–Nb–Si system is given in Fig.8. Therefore, the liquidus projection together with the reaction scheme of the whole ternary system was constructed for the first time. Although the data are tentative and further experiments are required to validate the prediction, they provide key information for alloy processing, e.g., composition design and selection of smelting temperature.

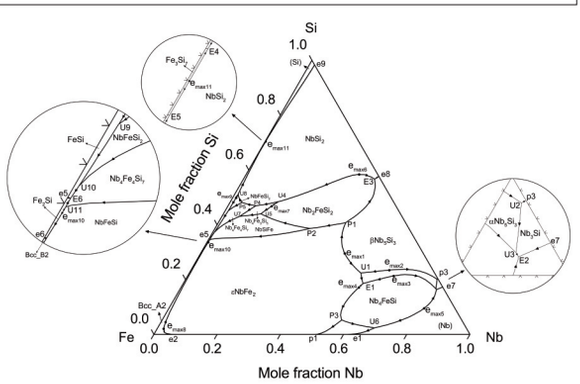

Figure 7. *Calculated liquidus projection of the Fe–Nb–Si system*

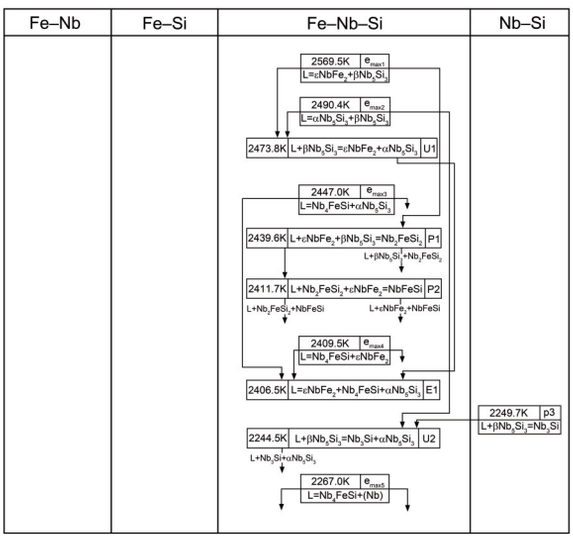

a

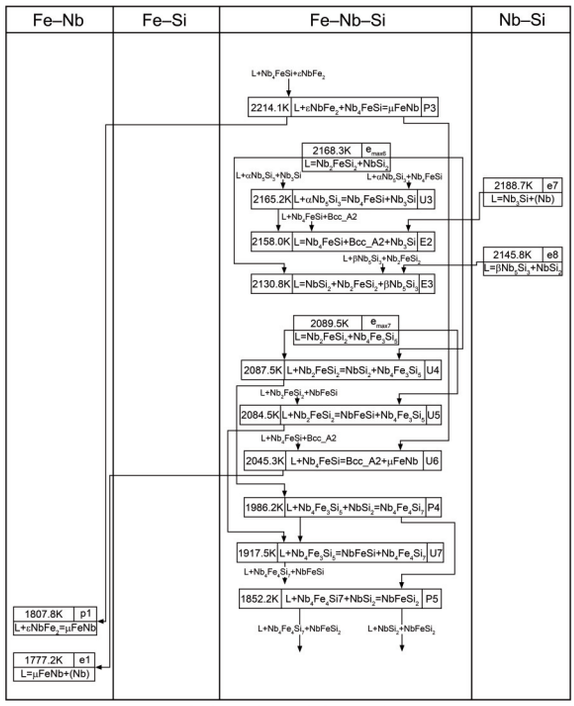

b (continued from a)

c (continued from b)

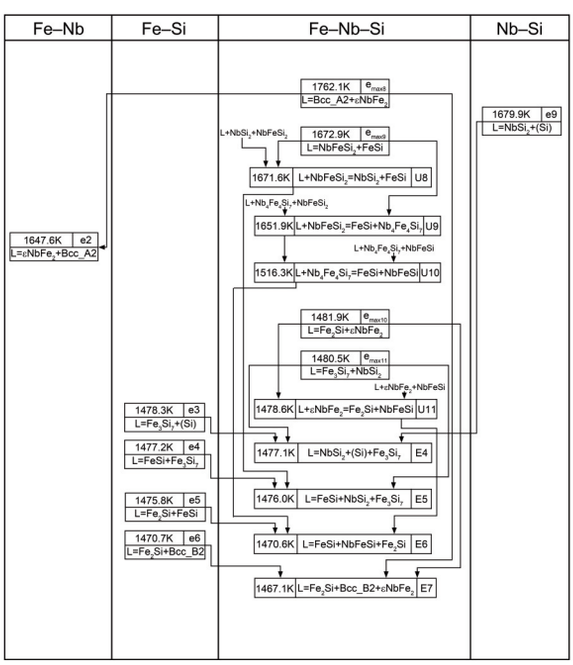

Figure 8. *Invariant reaction scheme for the Fe–Nb–Si system*

5. Conclusion

Based on the reliable experimental data, the Fe–Nb–Si system was thermodynamically investigated via the CALPHAD approach for the first time. The lattice constants and formation enthalpies of ternary compounds in this system were calculated by *ab initio* calculations, which serve as the supplement to the lack of experimental value. A set of self-consistent thermodynamic parameters was obtained. The calculated isothermal sections showed reasonable agreements with the experimental data at 1473, 1373, and 1273K, respectively. The calculated liquidus projection and invariant reaction scheme can provide useful guidance for alloy processing.

Acknowledgements

This research was funded by the Opening Foundation of the State Key Laboratory of Rare Metals Special Materials (Grant No. SKL2018K001), the "13th Five-Year" equipment pre-research and sharing technology project, grant numbers (Grant No. 41423040206), the National Science and Technology Major Project "Aero engine and Gas Turbine" (Grant No. 2017-VII-0008-0102) and the Natural Science Foundation of Zhejiang Province (LQ20E010004). K. Chang acknowledges the National Natural Science Foundation of China (51971235) and the CAS Pioneer Hundred Talents Program.

References

[1] B.P. Bewlay, M.R. Jackson, M.F.X. Gigliotti, Intermetallic Compounds-Principles and Practice (Edited by R.L. Fleischer and J.H. Westbrook), Vol. 3 (John Wiley & Sons) (2002).

[2] B.P. Bewlay, M.R. Jackson, J.C. Zhao, P.R. Subramanian, Metall. Mater. Trans. A, 34 (2003) 2043-2052.

[3] B.P. Bewlay, M.R. Jackson, J.C. Zhao, P.R. Subramanian, M.G. Mendiratta, J.J. Lewandowski, MRS Bull., 28 (2003) 646-653.

[4] P.R. Subramanian, M.G. Mendiratta, D.M. Dimiduk, JOM, 48 (1996) 33-38.

[5] P.R. Subramanian, M.G. Mendiratta, D.M. Dimiduk, M.A. Stucke, Mater. Sci. Eng. A, 239-240 (1997) 1-13.

[6] J.C. Zhao, J.H. Westbrook, MRS Bull., (2003) 622-630.

[7] M.R. Jackson, B.P. Bewlay, J.C. Zhao, General Electric Company, America (2003).

[8] S. Shin, R. Schäfer, B.C. De Cooman, Metall. Mater. Trans. A, 44 (2013) 4239-4247.

[9] M.E. McHerry, M.A. Willard, D.E. Laughlin, Prog. Mater. Sci., 44 (1999) 291-433.

[10] S.S. Campos, E.V. Morales, H.J. Kestenbach, Metall. Mater. Trans. A, 32 (2001).

[11] M. Jahazi, B. Eghbali, J. Mater. Process. Technol., 113 (2001) 594-598.

[12] D.K. Matlock, J.G. Speer, Mater. Sci. Technol., 25 (2009) 1118-1125.

[13] M. Negache, K. Taibi, N. Souami, H. Bouchemel, R. Belkada, Intermetallics, 36 (2013) 73-80.

[14] S. Sankaran, V. Subramanya Sarma, V. Kaushik, K.A. Padmanabhan, J. Mater. Process. Technol., 139 (2003) 642-647.

[15] D. Huang, S. Liu, Y. Du, Calphad, 68 (2020) 101693.

[16] M. Lou, X. Chen, K. Xu, Z. Deng, L. Chen, J. Lv, K. Chang, L. Wang, Acta Mater., 205 (2021) 116545.

[17] K. Xu, S. Liu, K. Chang, Y. Liang, Y. Du, Z. Jin, J. Magnes. Alloy., 9 (2021) 144-155.

[18] H.J. Goldschmidt, J. Iron Steel Inst., 194 (1960) 169-1800.

[19] J. Steinmetz, J.M. Albrecht, M. Zanne, B. Roques, Compt. Rend., 281 (1975) 831-833.

[20] J. Steinmetz, B. Roques, A. Courtois, J. Protas, Acta Crystallogr., 35B (1979) 2509-2514.

[21] B. Malaman, J. Steinmetz, G. Venturini, B. Roques, J. L.-Common Met., 87 (1982) 31-43.

[22] E.I. Gladyshevskii, Y.B. Kuz'ma, Zh. Strukt. Khim., 6 (1965) 991-993.

[23] V.Y. Markiv, Acta Crystallogr., A21 (1966) 84-87.

[24] W. Jeitschko, A.G. Jordan, P.A. Beck, Tran. Metall. AIME, 245 (1969) 335-339.

[25] F.X. Spiegel, D. Bardos, P.A. Beck, Tran. Metall. AIME, 227 (1963) 575-579.

[26] A.W. Denham, J. Iron Steel Inst., (1967) 435-436.

[27] B.N. Singh, K.P. Gupta, Metall. Trans., 3 (1972) 1427-1431.

[28] V. Raghavan, G. Ghosh, Trans. Indian Inst. Met., 37 (1984) 421-425.

[29] K.C. Hari Kumar, V. Raghavan, J. Alloy Phase Diagr., 5 (1989) 77-96.

[30] G. Haour, F. Mollard, B. Lux, I.G. Wright, Z. Metallkd., 69 (1978) 26-32.

[31] E. Paul, L.J. Swartzendruber, Bull. Alloy Phase Diagr., 7 (3) (1986) 248-254.

[32] W. Huang, Z. Metallkd., 81 (1990) 397-404.

[33] G.C. Coelho, S.G. Fries, H.L. Lukas, P. Majewski, J.M.Z. Bejarano, S. Gama, C.A. Ribeiro, G. Effenberg, Klaus Schulze Symp. Process. Appl. High Purity Refract. Met. Alloys, Proc. Symp., Eds. P. Kumar, H.A. John, and M. Uz, The Minerals, Metals, and Materials Society, Warrendale, Pa. USA (1994) 51-70.

[34] M. Mathon, D. Connétable, B. Sundman, J. Lacaze, Calphad, 33 (2009) 136-161.

[35] S. Srikanth, A. Petric, Z. Metallkd., 85 (1994) 164-170.

[36] C. Toffolon, C. Servant, Calphad, 24 (2000) 97-112.

[37] S.H. Liu, B. Hallstedt, D. Music, Y. Du, Calphad, 38 (2012) 43-58.

[38] A.V. Khvan, B. Hallstedt, Calphad, 39 (2012) 62-69.

[39] A.V. Khvan, B. Hallstedt, Calphad, 40 (2013) 10-15.

[40] O. Kunbaschewski, Iron-Binary Phase Diagrams", p. 32, Springer-Verlag, Berlin, (1982).

[41] J. Lacaze, B. Sundman, Metall. Trans. A, 22 (1991) 2211-2223.

[42] J. Miettinen, Calphad, 22 (1998) 231-256.

[43] I. Ohnuma, S. Abe, S. Shimenouchi, T. Omori, R. Kainuma, K. Ishida, ISIJ Int., 52 (2012) 540-548.

[44] S.L. Cui, I.H. Jung, Calphad, 56 (2017) 108-125.

[45] M.E. Schlesinger, H. Okamoto, A.B. Gokhale, R. Abbaschian, J. Ph. Equilib., 14 (1993) 502-509.

[46] H. Liang, Y.A. Chang, Intermetallics, (1999) 561-570.

[47] P.B. Fernandes, G.C. Coelho, F. Ferreira, C.A. Nunes, B. Sundman, Intermetallics, 10 (2002) 993-999.

[48] Y. Yang, Y.A. Chang, J.C. Zhao, B.P. Bewlay, Intermetallics, 11 (2003) 407-415.

[49] G. Shao, Intermetallics, 12 (2004) 655-664.

[50] G. Shao, Intermetallics, 13 (2005) 69-78.

[51] N. David, Y. Cartigny, T. Belmonte, J.M. Fiorani, M. Vilasi, Intermetallics, 14 (2006) 464-473.

[52] T. Geng, C. Li, J. Bao, X. Zhao, Z. Du, C. Guo, Intermetallics, 17 (2009) 343-357.

[53] T. Geng, C.R. Li, X.Q. Zhao, H.B. Xu, Z.M. Du, C.P. Guo, Calphad, 34 (2010) 363-376.

[54] Y. Li, C. Li, Z. Du, C. Guo, Calphad, 43 (2013) 112-123.

[55] X.J. Liu, H. Luo, Y. Lu, J.J. Han, J. Li, Y.H. Guo, Y.X. Huang, C.P. Wang, J. Phase Equilibria Diffus., 38 (2017) 897-905.

[56] C.A. Utton, I. Papadimitriou, H. Kinoshita, P. Tsakiropoulos, J. Alloys Compd. , 717 (2017) 303-316.

[57] L. Kaufman, Calphad, 3 (1979) 275-291.

[58] D. Wang, S.Y. Yang, M.J. Yang, J.P. Zheng, H.F. Hu, X.J. Liu, C.P. Wang, J. Alloys Compd. , 605 (2014) 183-192.

[59] A.T. Dinsdale, Calphad, 15 (1991) 317-425.

[60] O. Redlich, A.T. Kister, Ind. Eng. Chem., 40 (1948) 341-345.

[61] J.O. Andersson, T. Helander, L. Höglund, P. Shi, B. Sundman, Calphad, 26 (2002) 273-312.

[62] L. Chen, Z. Zhang, Y. Huang, J. Cui, Z. Deng, H. Zou, K. Chang, Calphad, 64 (2019) 225-235.

[63] K. Xu, L. Chen, K. Chang, P. Wan, M. Li, Z. Deng, F. Huang, Q. Huang, Calphad, 68 (2020) 101738.

[64] J.P. Perdew, K. Burke, M. Ernzerhof, Phys. Rev. Lett, 77 (1996) 3865-3868.

[65] G. Kresse, D. Joubert, Phys. Rev. B, 59 (1999) 1758-1775.

[66] G. Kresse, J. Furthmüller, Phys. Rev. B, 54 (1996) 11169-11186.

[67] H.J. Monkhorst, J.D. Pack, Phys. Rev. B, 13 (1976) 5188-5192.

TERMODINAMIČKO ODREĐIVANJE Fe–Nb–Si SISTEMA

Y. Jiang[a,c], F. Li[a,*], S.-R. Li[b,], K. Xu[c,***], L.-L. Chen[c], Z.-X- Deng[c], Y.-Y Huang[c], K. Chang[c]**

[a] Glavna termodinamička laboratorija za visokotemperaturne materijale i precizno oblikovanje, Univerzitet Đao Tong u Šangaju, Šangaj, Kina

[b] Glavna državna laboratorija za materijale od retkih metala, Severozapadni institut za istraživanje materijala od retkih metala Ningxia Co. Ltd., Šizuišan, Kina

[c] Glavna laboratorija za morske materijale i srodne tehnologije, Glavna laboratorija za morske materijale i zaštitnu tehnologiju, Institut za inženjerstvo i tehnologiju materijala u Ningbou, Ningbo, Džeđang, Kina

Apstrakt

Legure na bazi Nb – Si privlače sve veću pažnju zbog svojih odličnih mehaničkih svojstava na visokim temperaturama. Dodatak Fe bi mogao poboljšati njihovu lošu otpornost na oksidaciju na visokim temperaturama što u velikoj meri ograničava njihovu primenu. U cilju proučavanja uticaja dodavanja Fe u Nb – Si sistem i dizajniranja odgovarajućeg sastava legura, Fe–Nb–Si ternarni sistem je termodinamički ispitan primenom CALPHAD (CALculation of PHAse Diagrams) pristupa koji je dodatno potpomognut vrednostima entalpijama formiranja za ternarna jedinjenja na temperaturi od 0 K, koje su izračunate pomoću ab initio proračuna. Dobijen je samokonzistentan termodinamički opis Fe–Nb–Si sistema. Predstavljeni su i ključni izotermni preseci, kao i projekcija likvidusa, a rezultati proračuna su pokazali dobro slaganje sa dostupnim eksperimentalnim podacima.

Ključne reči: *Fe–Nb–Si; Fazni dijagram; CALPHAD; Ab initio proračun*